Journal of Biomechanics 65 (2017) 12–22

Contents lists available at ScienceDirect

Journal of Biomechanics

journal homepage: www.elsevier.com/locate/jbiomech
www.JBiomech.com

Red blood cell motion and deformation in a curved microvessel

Ting Ye [a,*], Nhan Phan-Thien [b], Chwee Teck Lim [b,c,d], Yu Li [a]

[a] Department of Computational Mathematics, Jilin University, China
[b] Department of Mechanical Engineering, National University of Singapore, Singapore
[c] Department of Biomedical Engineering, National University of Singapore, Singapore
[d] Mechanobiology Institute, National University of Singapore, Singapore

ARTICLE INFO

Article history:
Accepted 25 September 2017

Keywords:
Smoothed dissipative particle dynamics
Immersed boundary method
Secondary flow
Dean vortices
Red blood cell
Curved microvessel

ABSTRACT

The flow of cells through curved vessels is often encountered in various biomedical and bioengineering applications, such as red blood cells (RBCs) passing through the curved arteries in circulation, and cells sorting through a shear-induced migration in a curved channels. Most of past numerical studies focused on the cell deformation in small straight microvessels, or on the flow pattern in large curved vessels without considering the cell deformation. However, there have been few attempts to study the cell deformation and the associated flow pattern in a curved microvessel. In this work, a particle-based method, smoothed dissipative particle dynamics (SDPD), is used to simulate the motion and deformation of a RBC in a curved microvessel of diameter comparable to the RBC diameter. The emphasis is on the effects of the curvature, the type and the size of the curved microvessel on the RBC deformation and the flow pattern. The simulation results show that a small curved shape of the microvessel has negligible effect on the RBC behavior and the flow pattern which are similar to those in a straight microvessel. When the microvessel is high in curvature, the secondary flow comes into being with a pair of Dean vortices, and the velocity profile of the primary flow is skewed toward the inner wall of the microvessel. The RBC also loses the axisymmetric deformation, and it is stretched first and then shrinks when passing through the curved part of the microvessel with the large curvature. It is also found that a pair of Dean vortices arise only under the condition of $De > 1$ (De is the Dean number, a ratio of centrifugal to viscous competition). The Dean vortices are more easily observed in the larger or more curved microvessels. Finally, it is observed that the velocity profile of primary flow is skewed toward the inner wall of curved microvessel, i.e., the fluid close to the inner wall flows faster than that close to the outer wall. This is contrary to the common sense in large curved vessels. This velocity skewness was found to depend on the curvature of the microvessel, as well as the viscous and inertial forces.

1. Introduction

The flow of cells through curved vessels is often encountered in various biomedical and bioengineering applications, such as RBCs passing through the curved arteries in circulation, and cells sorting by shear-induced migration in a curved channels. It is broadly accepted in biomedical community that the curved shape of the vessel may play a critical role in the development of some diseases, for example, atherosclerosis particularly prevalent on the inner wall of curved arteries (Lee et al., 2008). In bioengineering applications, the curved flow effects may lead to cross-streamline cells' migration, which has been explored in sorting and manipulating cells, like the spiral bio-chip for the enrichment or separation of circulating tumor cells (CTCs) (Hou et al., 2013; Warkiani et al., 2014a,b, 2016).

Most of the previous numerical studies on flows of RBCs focused on cells' motion (Lac et al., 2004; Sui et al., 2008; Hosseini and Feng, 2009; Noguchi, 2009; Bagchi and Kalluri, 2009; Noguchi, 2010; Ye et al., 2010, 2014b; Yazdani and Bagchi, 2011; Bagchi and Kalluri, 2011), their deformation (Dao et al., 2003; Fedosov et al., 2010; Ye et al., 2013), aggregation (Liu et al., 2004; Bagchi et al., 2005; Zhang et al., 2008; Li et al., 2014) and rheology (Pries et al., 1992; Bagchi, 2007; Doddi and Bagchi, 2009; Zhang, 2011; Xu et al., 2013; Ye et al., 2014a). The microvessel is often assumed straight and uniformly-sized rectangular or cylindrical tubes. The flow generated is either shear or Poiseuille flow, by moving the microvessel wall or by applying an external force to fluid; and then the RBCs behavior is studied. It has been reported that, roughly speaking, there are three typical motions of a RBC

* Corresponding author.
E-mail address: yeting@jlu.edu.cn (T. Ye).

https://doi.org/10.1016/j.jbiomech.2017.09.027
0021-9290/

in simple shear flow: tank-treading, trembling and tumbling motions for the steady, transition and unsteady states, respectively (Sui et al., 2008; Noguchi, 2009; Yazdani and Bagchi, 2011; Dupire et al., 2012; Luo et al., 2013; Lanotte et al., 2016), and two typical motions in Poiseuille flow: symmetric motion with parachute deformation and asymmetric motion with slipper deformation (Pozrikidis, 2005; Kaoui et al., 2009; Tahiri et al., 2013). There have also been many numerical studies (Bagchi et al., 2005; Liu and Liu, 2006; Zhang et al., 2008, 2009; Doddi and Bagchi, 2009; Wang et al., 2009; Gong et al., 2009; Takagi et al., 2009; McWhirter et al., 2009; Noguchi et al., 2010; McWhirter et al., 2011; Fedosov et al., 2013; Xu et al., 2014) on the aggregation and dissociation of RBCs in shear and Poiseuille flows, as well as their effects on the blood rheological properties. These studies are mainly motivated by some diseases found in blood microcirculation, such as sickle cell anemia and thrombus, and often assume a straight vessel. On the other hand, the human vasculature is a complex network with curved and bifurcated vessels. One of the first curved vessels encountered by blood on its exit from the heart is the aortic arch. This curved shape enables the blood ejected from the heart to reverse and move in a caudal direction toward the body, which, in turn, affects the forces acting on the inner lining of the vessels, possibly leading to arterial diseases (Chandran et al., 2007). Hence, the aortic arch is the subject in most past studies on curved vessels (Shahcheraghi et al., 2002; Morris et al., 2005; Vincent et al., 2011; Konoura et al., 2013; Nardi and Avrahami, 2017). The main difference suggested from these studies between straight and curved vessels is that the latter may cause a development of a secondary flow as well as a skewness in the primary flow velocity profile. Such flow pattern may be one of the major reasons for the occurrence of arterial diseases. In addition, curved tubes have also been used to design microfluidic chips based on the associated curved flow patterns, which can be utilized to sort and manipulate cells (Hou et al., 2013; Warkiani et al., 2014a,b, 2016). The chip is usually designed to be relatively large for a high throughput, i.e., high efficiency in cell manipulation. Thus, one can find that the size of the curved vessel in most past studies is relatively large, about 100 μm even to 1 cm in diameter, in the flow simulation in aortic arch or in a microfluidic chip. In such curved vessels, the cell deformation has not been taken into account. Hence, a valuable consideration is what can happen if cells pass through a curved capillary with a diameter comparable to a cell diameter, where the cell deformation must be considered. More recently, Bagchi's group (Vahidkhah et al., 2016; Balogh and Bagchi, 2017) used the immersed boundary method (IBM) to study the cellular-scale blood flow in complex geometry, including the stenosed and bifurcated microvessels, and even the microvascular network rendered from an *in vivo* image.

This work aims to numerically investigate the motion and deformation of a RBC in a curved microvessel using the SDPD method. Particularly, we focus on the effects of curvatures, the types and sizes of the curved microvessel on the RBC deformation and the associated flow pattern.

2. Models and methods

We consider the motion of a RBC along the centerline of a curved microvessel, with a length L, a circular cross section of radius R_v and a height H_c (from the centerline to the baseline), as illustrated in Fig. 1(a). The RBC's interior is filled with cytoplasm fluid, and suspended in the medium fluid. It is assumed that both fluids are incompressible and Newtonian, and the flow is isothermal. Furthermore, it is assumed that they have the same density and viscosity, which is one of shortcomings of the present work. The previous studies (Ye et al., 2014b) have shown that the cells may move slower and its deformation will be smaller if considering the contrasts of density and viscosity. Therefore, the motion of the fluids in the interior, and exterior of the RBC is governed by

$$\nabla \cdot \boldsymbol{v} = 0, \tag{1}$$

$$\rho \frac{d\boldsymbol{v}}{dt} = -\nabla P + \eta \nabla^2 \boldsymbol{v} + \rho \boldsymbol{g} + \boldsymbol{f}, \tag{2}$$

where ρ, η, $\boldsymbol{v}$ and P are the density, viscosity, velocity and pressure of fluid, t is the time, and $\boldsymbol{g}$ is the gravity that drives the fluid flow; $\boldsymbol{f}$ is the singular force generated when treating the fluid-RBC interaction using the IBM (Peskin, 2002), where the RBC membrane is treated as a surface boundary immersed in the fluid, and it is given by

$$\boldsymbol{f}(\boldsymbol{x}, t) = \int_{\Gamma} \boldsymbol{F}_d(r, s, t)\delta(\boldsymbol{x} - \boldsymbol{X}(r, s, t))drds, \tag{3}$$

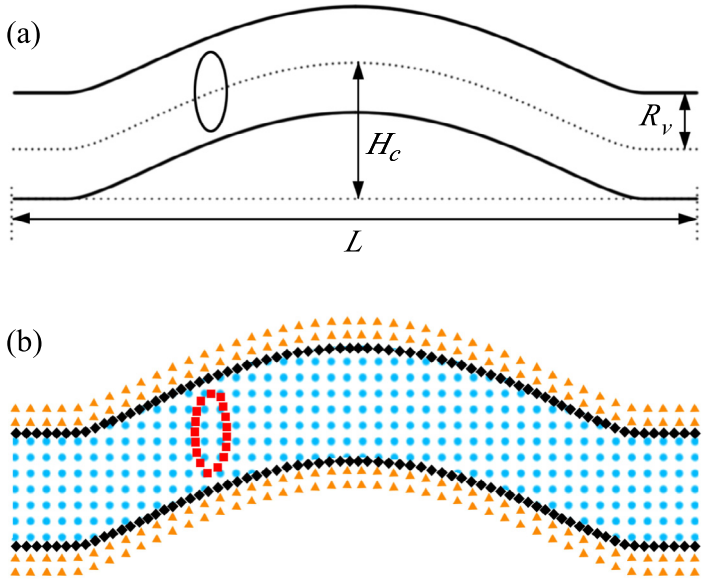

Fig. 1. Problem description, (a) schematic illustration of a cell moving through a microvessel, (b) particle representation of simulation domain, including fluid particles (circles), type-1 boundary particles (diamonds), type-2 boundary particles (triangles) and membrane particles (squares).

$$\frac{d\boldsymbol{X}}{dt} = \int_{\Omega} \boldsymbol{v}(\boldsymbol{x},t)\delta(\boldsymbol{x} - \boldsymbol{X}(r,s,t))d\boldsymbol{x}, \tag{4}$$

where Γ is the closed surface of the RBC membrane, Ω is the spatial domain of simulation, (r,s) is the curvilinear coordinate to define a point on the RBC membrane, $\boldsymbol{X}$ is the spatial coordinate of the RBC membrane, $\boldsymbol{x}$ is a spatial coordinate of fluid, $\boldsymbol{F}_d$ is the force density (per unit area) acting on an area of the RBC membrane, and δ is the Delta Dirac function. An additional equation of state (EOS) relating pressure to density is required to close the Eqs. (1)–(4). Following previous studies (Morris et al., 1997, 2000), we here adopt an EOS with the simple form

$$P = \rho c^2, \tag{5}$$

where c is the artificial sound speed. It is chosen appropriately, enough large to ensure that the simulating fluid has a similar compressibility to a real fluid, yet not so large to make the time step prohibitively small.

The SDPD method (Español and Revenga, 2003) is applied to numerically discretize the Eqs. (1)–(5). The fluid interior and exte-

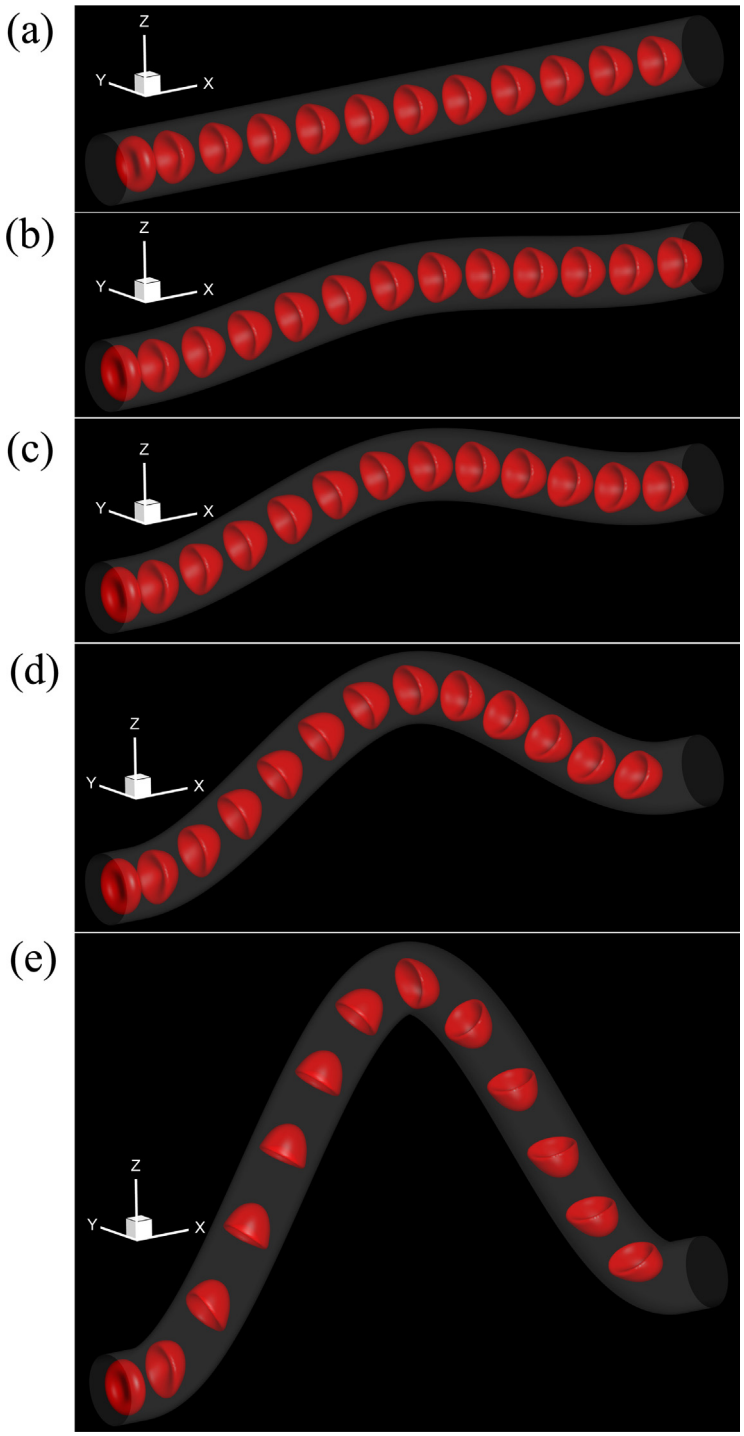

Fig. 2. The shape evolution of an RBC in a microvessel of heights, $H_c = 0$ (a), 5 (b), 10 (c), 20 (d) and 50 μm (e), respectively. Snapshots, from left to right, are taken from $t = 0$ ms with an interval of 0.62 ms.

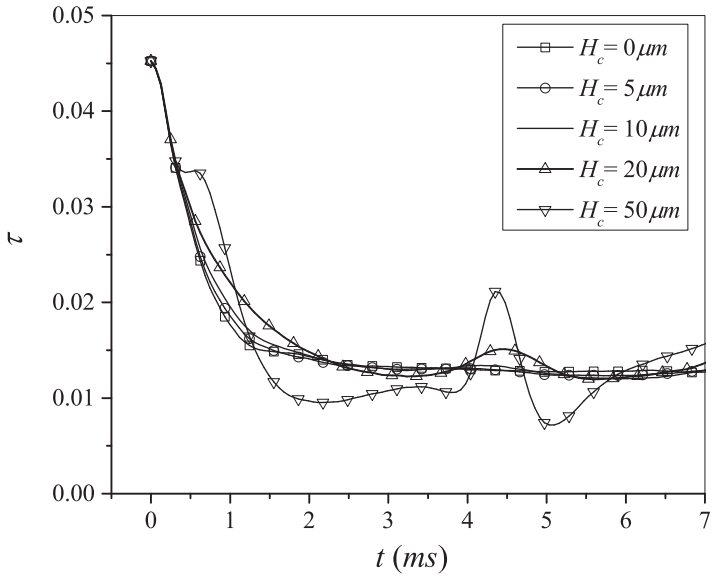

Fig. 3. The asphericity of an RBC in the microvessel with different heights H_c.

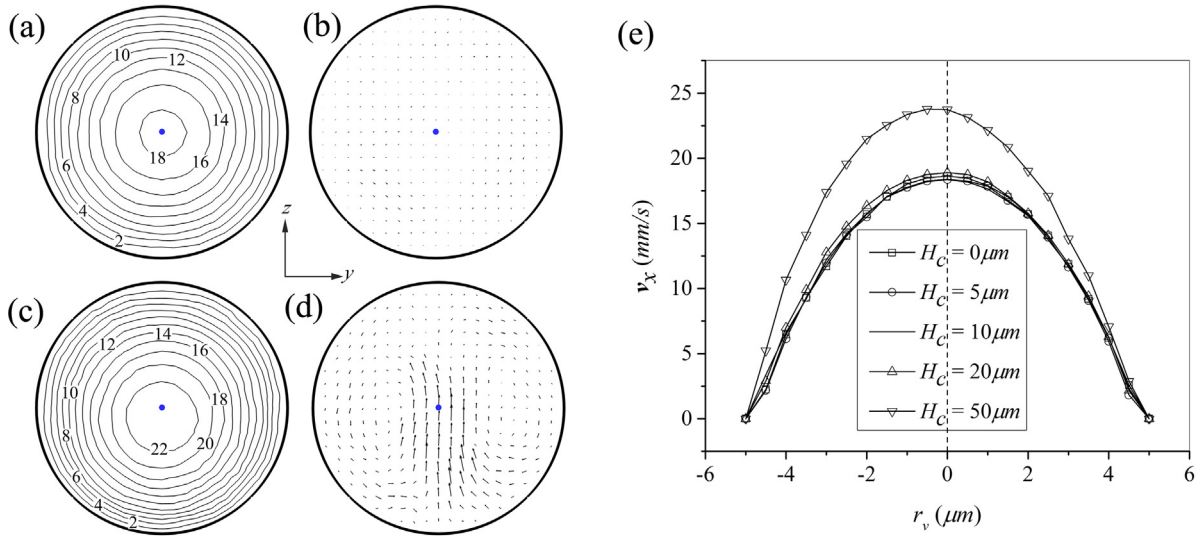

Fig. 4. Velocity distribution on the cross-section normal to the centerline, extracted at the microvessel summit, including contours of the axial velocity (with unit of mm/s) at $H_c = 0$ (a) and 50 μm (c), vectors of the radial velocity at $H_c = 0$ (b) and 50 μm (d), and profiles of axial velocity at the different heights H_c (e). The solid point is the center of cross-section, and the dash line is $r_v = 0$ μm, served as a reference point and a reference line, respectively.

rior of the RBC are represented by a set of discrete particles, as shown in Fig. 1(b), and each of particle associates with physical properties, such as mass, velocity and density. Based on the SDPD formulation (Español and Revenga, 2003), we can write the fluid governing equations as

$$\frac{d\boldsymbol{x}_i}{dt} = \boldsymbol{v}_i, \tag{6}$$

$$m\frac{d\boldsymbol{v}_i}{dt} = \sum_j \left[\alpha_{ij}\boldsymbol{x}_{ij} - \gamma_{ij}\left(\boldsymbol{v}_{ij} + (\boldsymbol{e}_{ij}\cdot\boldsymbol{v}_{ij})\boldsymbol{e}_{ij}\right) + (A_{ij}/dt)\widehat{d\boldsymbol{W}}_{ij}\cdot\boldsymbol{e}_{ij}\right] + m\boldsymbol{g}_i + \boldsymbol{f}_i, \tag{7}$$

the IBM formulations as

$$\boldsymbol{f}_i = \sum_k \beta_{ik}\boldsymbol{F}_k, \quad \frac{d\boldsymbol{X}_k}{dt} = \sum_i \beta_{ik}\boldsymbol{v}_i, \tag{8}$$

and the EOS as

$$P_i = md_ic^2. \tag{9}$$

The detailed expressions of each coefficient can be found in Supplementary Material. These equations from (6)–(9) are numerically solved by the velocity-Verlet algorithm (Groot and Warren, 1997), due to its high computational efficiency.

3. Results and discussions

3.1. Simulation conditions

We here describe the simulation conditions for a benchmarking case, where the tube size is $L = 100$ μm, $R_v = 5$ μm and $H_c = 10$ μm, and the RBC is described by Evans and Fung (1972)

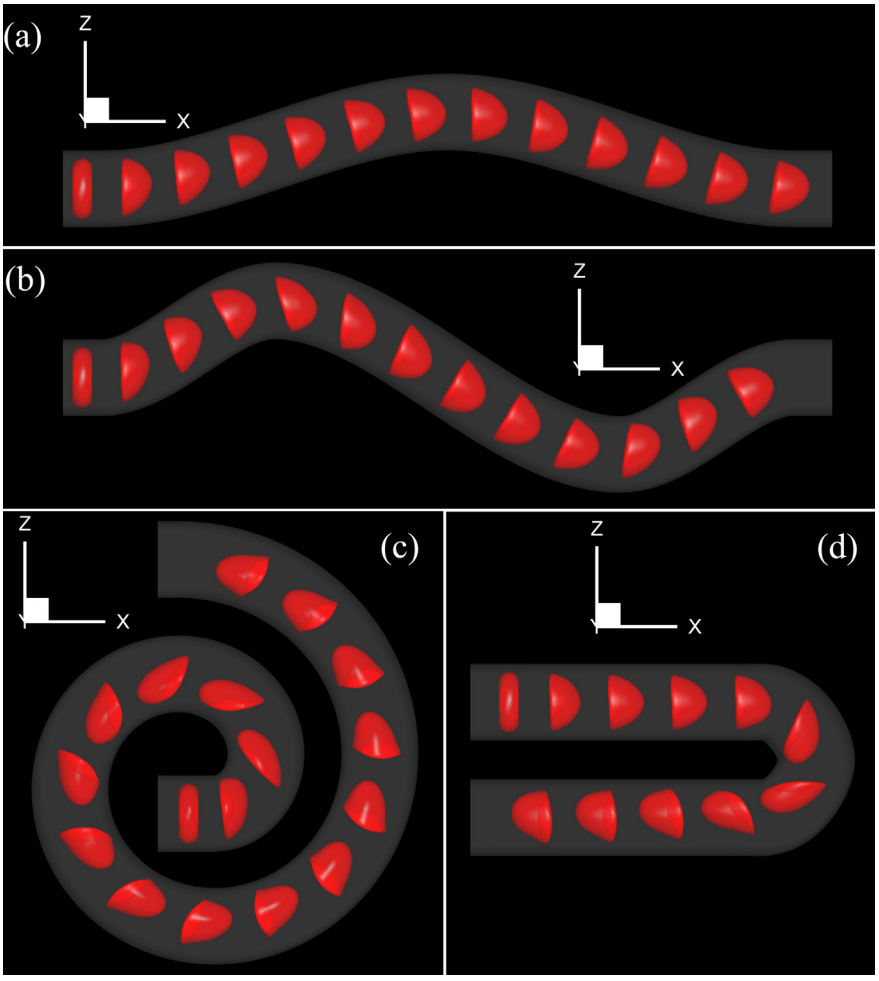

Fig. 5. Shape evolution of RBC in the arch (a), ripple (b), spiral (c) and U-bend (d), where the snapshots of the RBC are taken,from the inlet to outlet, from $t = 0$ ms with an interval of 0.62 ms.

$$z = \pm\sqrt{1-\frac{x^2+y^2}{R^2}}\left[C_0 + C_1\frac{x^2+y^2}{R^2} + C_2\frac{(x^2+y^2)^2}{R^4}\right], \tag{10}$$

with the parameters $R = 3.91$ μm, $C_0 = 0.81$ μm, $C_1 = 7.83$ μm and $C_2 = -4.39$ μm. The surface area and volume of this RBC are 135 μm^2 and 94 μm^3. The fluid has the following physical properties: density $\rho = 10^3$ kg/m^3, viscosity $\eta = 10^{-4}$ Pa s, and Boltzmann temperature $k_BT = 4.14\times10^{-21}$ J. The RBC has the following mechanical properties: shear modulus $E_s = 6.0\times10^{-6}$ N/m, and bending modulus $E_b = 2.0\times10^{-19}$ J, which are very close to experimental values (Hochmuth, 1987). To drive the system, an external force $\boldsymbol{g}$ is applied to the fluid, with the magnitude of 320 m/s^2 and assumed to be along the centerline of microvessel. The initial particle density is $d = 15.625$ μm^{-3}, the artificial sound speed is $c = 0.1$ m/s, and the time step is $\Delta t = 0.124$ μs. In the absence of the RBC, the fluid flow generated has the maximum velocity of about 0.02 m/s. The Reynolds number $Re = \rho u_m D_v/\eta \approx 1.0$, and the Mach number $Ma = u_m/c \approx 0.1$, where u_m is the mean velocity and D_v is the microvessel diameter. Note that both Re and Ma are much larger than the values in reality for saving the computational cost. This telescoped trick is often used in most of CFD methods for making the numerical simulation possible. The previous studies have shown that Re has a slight effect on the cell behavior under $Re < 10$ (Ye et al., 2017), and Ca has a negligible effect under $Ca < 0.3$ (Vázquez-Quesada et al., 2009). To evaluate the RBC deformation, moreover, we introduce a measure, called the asphericity defined as (Noguchi and Gompper, 2005)

$$\tau = \frac{1}{2}\frac{(I_1-I_2)^2+(I_2-I_3)^2+(I_3-I_1)^2}{(I_1+I_2+I_3)^2}, \tag{11}$$

where I_1, I_2 and I_3 are the principal moments of inertia; note that this measure approaches zero when the RBC becomes more and more spherical.

3.2. Curvatures of the microvessel

Fig. 2 shows the shape evolution of a RBC in the microvessel, with $H_c = 0$, 5, 10, 20 and 50 μm, respectively. The RBC deforms gradually into a domed shape. At $H_c = 0$ μm, the RBC deformation is axisymmetric, and this is maintained at $H_c = 5$ and 10 μm. At $H_c = 20$ and 50 μm, the RBC deformation is no longer axisymmetric, with the asymmetric deformation becomes more pronounced in the course of the RBC's motion through the curve microvessel. Fig. 3 shows the RBC's asphericity, which is almost same at $H_c = 0$, 5 and 10 μm, but different at $H_c = 20$ and 50 μm. This indicates that a mild curvature, at $H_c = 5$ and 10 μm, has almost no effect on the RBC deformation, but a larger curvature, at $H_c = 20$ and 50 μm, certainly affects the RBC deformation. Especially at $H_c = 50$ μm, the RBC asphericity first increases and then decreases, suggesting that the RBC is first stretched and then shrinks, when flowing through the summit of a curved microvessel. This change

of asphericity is here called a "unimodal" change for a clear description. Thus, the RBC has a unimodal change of asphericity when flowing through the summit of a curved microvessel, as shown in Fig. 3. The information of the RBC motion can be found in Supplementary Material.

In a flow through a curved microvessel, secondary flow arises because of the radial pressure gradient driving the fluid in the cross-section to move radially (Sollier et al., 2009). Fig. 4 shows the velocity distribution on the cross-section extracted at the microvessel summit. At $H_c = 0$ μm, the axial velocity is axisymmetric, with its maximum value at the centerline. A similar axial velocity profile is obtained at $H_c = 5$, 10 and 20 μm. At $H_c = 50$ μm, however, the axial velocity is no longer axisymmetric, and its maximum value is skewed toward the inner wall. In other words, the fluid close to the inner wall flows faster than that close to the outer wall. This is in contrast to the common sense in large curved vessels that the fluid close to the outer wall usually flows faster. Sun et al. (2013) attributed this velocity skewness to the balance between viscous and inertial competitions (Sun et al., 2013), characterized by the *Re* number. They explained that the surface area of the inner wall is smaller than the outer wall, and thus the fluid experiences less friction force from the inner wall than from the outer wall. With low *Re*, the viscous force (friction force) dominates the flow because of weak inertial effect, giving rise to a higher flow velocity near the inner wall, as shown in Fig. 4(c). As *Re* increases beyond a critical value, inertial effects dominate the flow, and thus the flow near the outer wall is stronger that near the inner wall. Sun et al. (2013) observed that the axial velocity is skewed to the inner wall at $Re < 17.16$, and to the outer wall at $Re > 52.45$. In our work, $Re \approx 1.0$, with the axial velocity skewed toward the inner wall. In most cases, however, $Re > 100$, and thus the axial velocity is skewed toward the outer wall. In order to quantitatively analyze it, we plot its profiles along the vertical centerline on the cross-section at the microvessel summit, i.e. $x = 0$ and $y = 0$, as shown in Fig. 4(e). At $H_c = 0$, 5, 10 and 20 μm, the axial velocity are almost same and symmetric, implying that the axial velocity is almost axisymmetric. Hence, the curved microvessel in these cases has negligible effect on the flow pattern. The axial velocity at $H_c = 50$ μm is not symmetric with respect to $r_v = 0$, and its maximum value is achieved below $r_v = 0$. This indicates that the fluid near the inner wall flows faster than that near the outer wall. A dimensionless number, called Dean number *De*, can be used to identify the effect of curvature on the flow structure. It is defined as $De = Re\sqrt{R_v/R_c}$ (Helin et al., 2009), where R_c is here the minimum curvature radius of the microvessel centerline. It describes the relative importance of centrifugal to viscous force. Our cases of $H_c = 0$, 5, 10, 20 and 50 μm correspond to $De = 0$, 0.272, 0.385, 0.544 and 1.033, respectively. When $De = 0$, there is no centrifugal effect, and thus no secondary flow is developed, as shown in Fig. 4(b). With increasing *De* (but $De < 1$), the centrifugal effect becomes stronger and stronger, yet not so strong to overcome the viscous force, and thus no secondary flow is observed. Until $De > 1$, the centrifugal effect plays a dominant role, i.e., the pressure near the inner wall is sufficiently larger than that near the outer wall (Sollier et al., 2009) generating a radial pressure gradient that drives a secondary flow. A pair of symmetrically swirling secondary vortices arise on the cross-section, so-called Dean vortices, as shown in Fig. 4(d).

3.3. Types of microvessels

Fig. 5 shows the shape evolution of RBC in the arch, ripple, spiral and U-bend microvessels. These microvessels are generated by sweeping a circle with the radius of $R_v = 5$ μm along the centerline in a pre-defined manner. It is obvious that the RBC deforms non-axisymmetric in these microvessels, especially at the position with the largest curvature. The conclusion drawn in the previous section shows that the fluid near the inner wall flows faster than

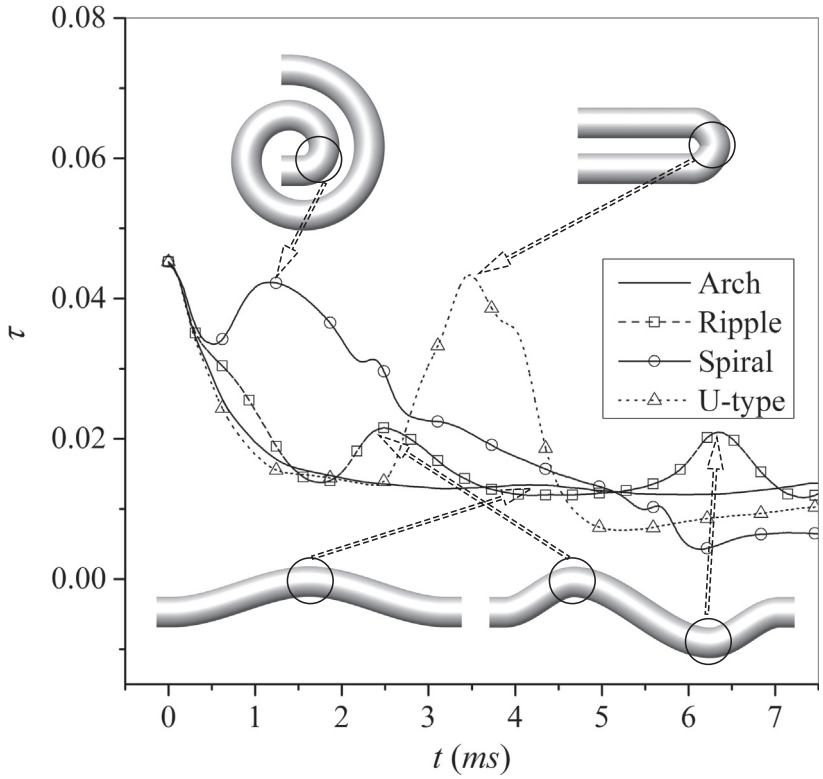

Fig. 6. Asphericities of RBC in the arch, ripple, spiral and U-bend microvessels, where the insets are to show the positions with the largest curvature.

that near the outer wall, at low *Re*, such that the part of RBC near the inner wall is pushed forward faster than the part near the outer wall. Hence, the RBC is stretched more at its position in the large curvature region, but less so at its position in the small curvature region. This leads to the unimodal variation of RBC asphericity at the position with the largest curvature, noted in Fig. 6. This is main feature of RBC deformation in a curved microvessel. The information of the RBC motion can be found in Supplementary Material. In addition, it is noted that the minimum radius of curvature is $R_c = 33.78,\ 8.432,\ 5.596$ and 3.065 μm for the arch, ripple, spiral and U-bend microvessels, and thus $De = 0.385,\ 0.770,\ 0.945$ and 1.192. Hence, the Dean vortices will be expected in the U-bend microvessel only, as shown in Fig. 7. There are two obvious Dean vortices emerging, and the maximum axial velocity is skewed toward the inner wall. Fig. 7(c) shows the profile of axial velocity on the cross-section extracted at the position with the largest curvature in each microvessel. It is almost axisymmetric with respect to $r_v = 0$ μm in the arch, ripple and spiral microvessels. This reflects the fact that the centrifugal force is insufficient to overcome the viscous force. In the U-bend microvessel, the axial velocity is no longer axisymmetric and skewed toward the inner wall, and the secondary flow is observed with the typical Dean vortices. This indicates that the centrifugal force is enhanced and exceeds the viscous force once $De > 1$, leading to the secondary flow.

3.4. Sizes of the microvessel

Fig. 8 shows the shape evolution of a RBC in a microvessel of different diameter values. Because the flow is driven by the same external force $\boldsymbol{g}$, the axial velocity increases as the diameter increases. This results in the RBC to be transported further in the larger microvessel during the same time interval. The deformation of RBC is also presented, as shown in Fig. 9. As $D_v = 8$ μm, the RBC moves to the summit of microvessel at about $t = 7.2$ ms, and thus its asphericity undergoes a unimodal change. At $t = 13.6$ ms, the RBC exits from the outlet and subsequently is placed back at the inlet, because we adopt the periodic boundary condition on the outlet and inlet. During this transition, the RBC actually goes through two neighboring curved parts, such that there should be two unimodal changes of the RBC asphericity. However, the relative curvatures (R_v/R_c) near the inlet and outlet are small because of the small R_v, and thus these two unimodal changes are not

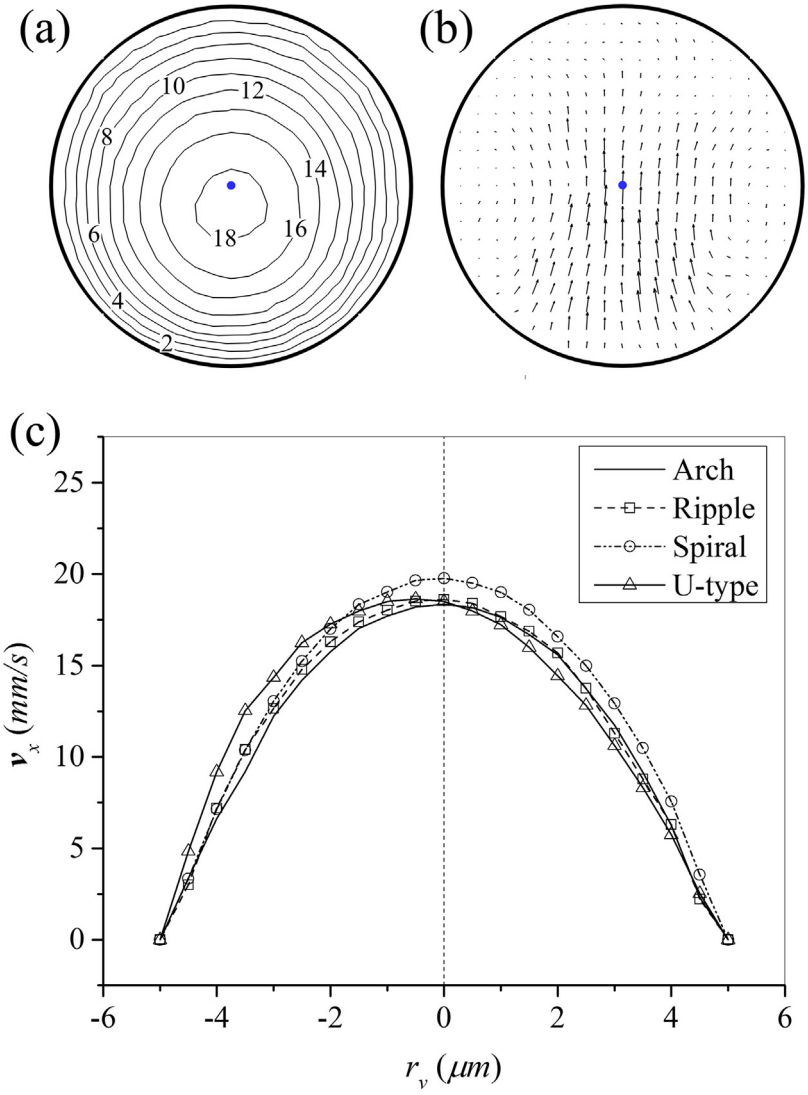

Fig. 7. Velocity distribution on the cross-section at the position with the largest curvature, including contours of the axial velocity (with unit of mm/s) in the U-bend microvessel (a), vectors of the radial velocity in the U-bend microvessel (b), and profiles of axial velocity in the different types of microvessels (c). The solid point is the center of cross-section, and the dash line is $r_v = 0$ μm, served as a reference point and a reference line, respectively.

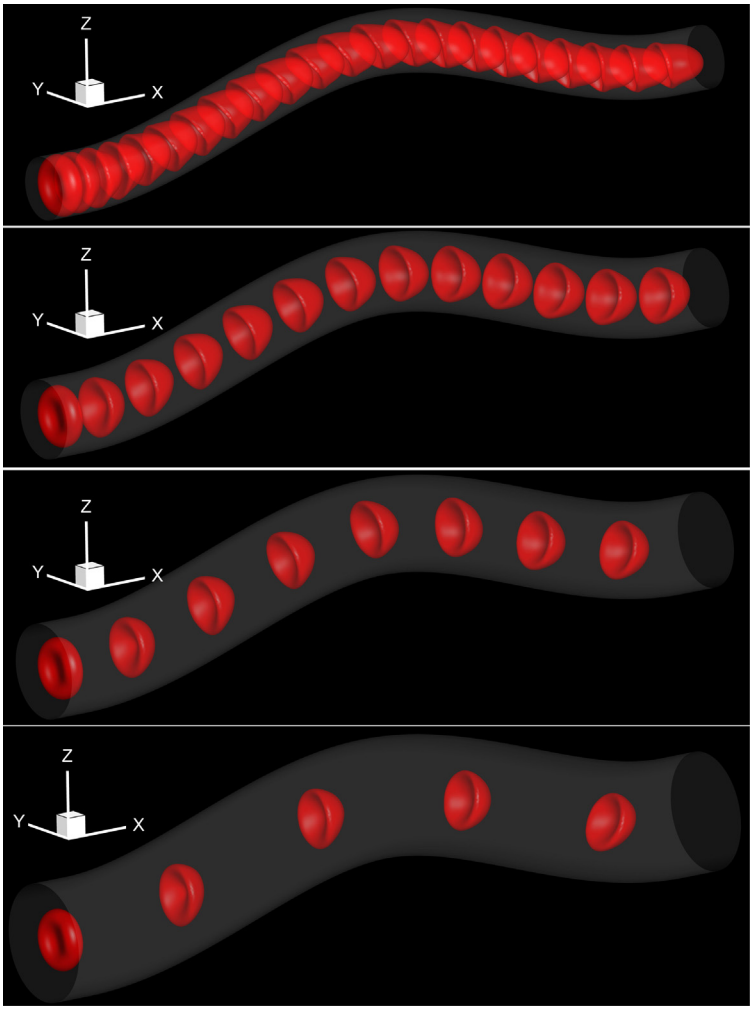

Fig. 8. Shape evolution of RBC in the arch microvessel, with different diameters, $D_v = 8$ (a), 10 (b), 12 (c) and 15 μm (d), where the snapshots of RBC from the inlet to outlet are taken from $t = 0$ ms with an interval of 0.62 ms.

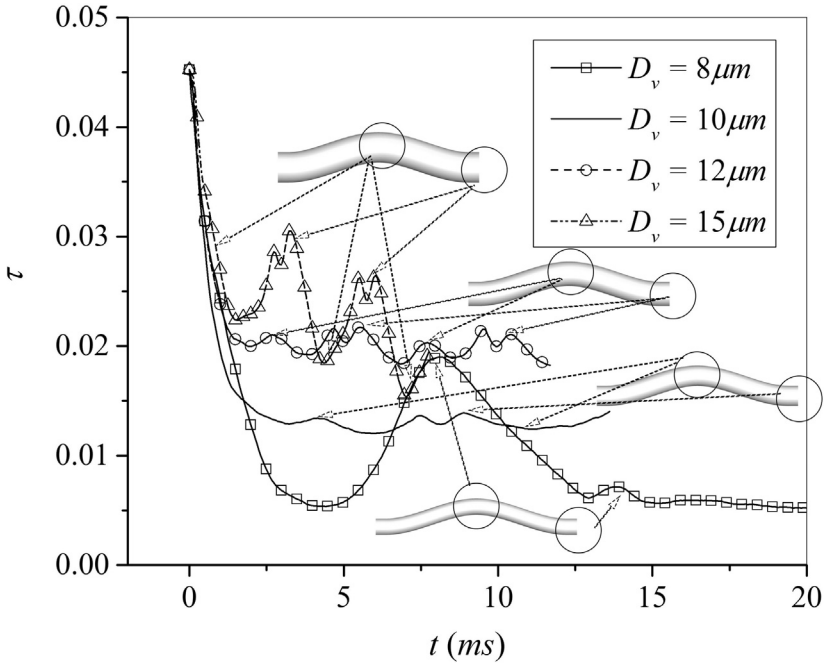

Fig. 9. Asphericities of RBC in the arch microvessels with the different diameters D_v.

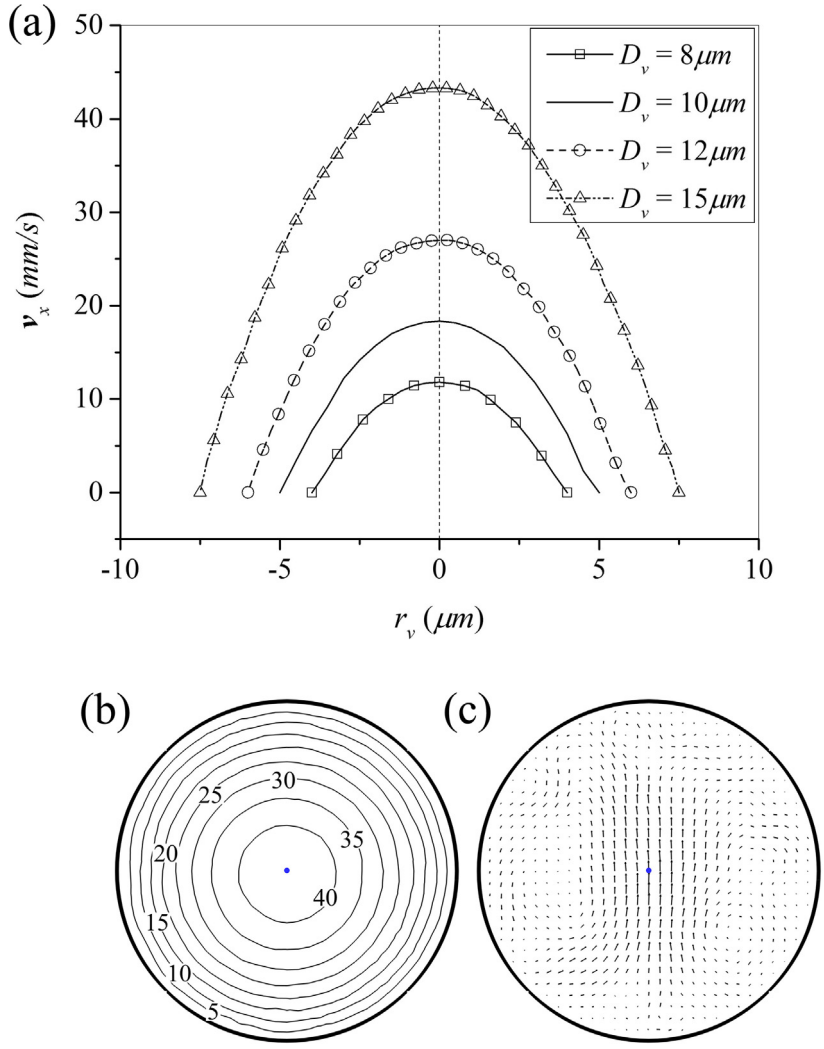

Fig. 10. Velocity distribution on the cross-section extracted at the summit of arch microvessel, including profiles of axial velocity at the different diameters D_v (a), contours of the axial velocity (with unit of mm/s) at $D_v = 15$ μm (b), and vectors of the radial velocity at $D_v = 15$ μm (c). The solid point is the center of cross-section, and the dash line is $r_v = 0$ μm, served as a reference point and a reference line, respectively.

obvious enough. As $D_v = 10$ μm, the RBC arrives to the summit at $t = 4$ ms, and to the outlet at $t = 7.9$ ms. After that, it comes back to the inlet, and to the summit again at $t = 11.8$ ms. As $D_v = 12$ μm, the RBC arrives at the summit at $t = 2.5$ and 7.3 ms for the first and second rounds, and to the outlet at $t = 4.9$ and 9.8 ms, respectively. As $D_v = 15$ μm, it arrives at the summit at $t = 1.45$, 4.23 and 7.02 ms for the first, second and third times, and to the outlet at $t = 2.8$ and 5.66 ms for the first and second times. The asphericity in the last three cases has the similar change as the first case that a unimodal change is observed when the RBC goes through every curved part. When two neighboring curved parts are quite close, for example, the curved parts near the inlet and outlet, two neighbouring unimodal changes make up a bimodal one. In the last case with $D_v = 15$ μm, this bimodal change is the most obvious. In addition, the asphericity increases as the diameter increases; in other words, the RBC is more squeezed in a smaller microvessel, especially at $D_v = 8$ μm. As the vessel diameter increases, the repulsion from the microvessel becomes less and less important. Hence, this increase of asphericity is not observed when the diameter increases from 12 to 15 μm. The information of the RBC motion can be found in Supplementary Material. Fig. 10(a) shows the axial velocity profile on the cross-section extracted at the microvessel summit, where it is almost axisymmetric in all four cases, and increases as the microvessel diameter increases. The Reynolds number and Dean number for these cases are, $Re = 0.472, 1.0, 1.621, 3.25$, and $De = 0.163, 0.385, 0.683, 1.531$, respectively. The secondary flow appears in the microvessel with $D_v = 15$ μm, as shown in Fig. 10 (b) and (c). However, the axial velocity is still axisymmetric. This is because the curvature of the microvessel here is not large enough to allow the fluid near the inner and outer walls experiences sufficiently different friction forces. Taking an extreme case for example, the axial velocity will be never skewed in a straight tube no matter how large *Re* is. Hence, a conclusion is drawn that the skewness of the axial velocity depends on the curvature of the microvessel, except the viscous and inertial forces.

4. Conclusions

This study is undertaken to gain an understanding of the motion and deformation of a RBC in a curved microvessel with a small diameter of about 10 μm (comparable to a RBC diameter), in which the Reynolds number is also quite small, of about 1.0. SDPD, a particle-based method, is used to simulate the fluid flow because of its great flexibility in handling complex structures, and IBM, a

commonly used fluid-structure treatment method, is employed to deal with the fluid-RBC interaction. We study the effects of curvature, the type and the size of the microvessel on the motion and deformation of RBC, as well as the associated flow pattern.

The simulation results show that the small curvature of the microvessel has negligible effect on the RBC behavior and the flow pattern. The flow structure is still dominated by a Poiseuille flow without a secondary flow, and thus the RBC behavior is almost the same as in a straight microvessel with an associated axisymmetric and parachute deformation. When the curvature of the microvessel is large enough, a secondary flow comes into being with a pair of Dean vortices, and the axial velocity profile is skewed toward the inner wall of the microvessel. The RBC is stretched during the period leading to the peak of curvature, but shrinks relatively during the subsequent period away from the peak curvature. Thus, its asphericity has an obvious unimodal shape, with an increase and then decrease, when it passes through a large curvature part of the microvessel. In addition, it is found that a pair of Dean vortices arise when $De > 1$, for example, in the arch microvessel with $H_c = 50\ \mu m$ or $D_v = 15\ \mu m$, and the U-bend microvessel. This leads to the appearance of a secondary flow pattern on the cross-section of the microvessel, associated with a pair of Dean vortices. Finally, it is also observed that the axial velocity is skewed toward the inner wall, i.e., the fluid close to the inner wall flows faster than that close to the outer wall. This is contrary to the fluid behavior in a large curved channel. This velocity skewness depends on the friction forces from the inner and outer wall, as well as the inertial forces. When the curvature of the microvessel is large enough, the surface area of the inner wall is much smaller than the outer wall, and thus the fluid experiences less friction force from the inner wall than from the outer wall. At the same time, if the inertial force is not much larger than the viscous force (i.e., small *Re*), the flow velocity near the inner wall becomes faster than that near the outer wall.

Conflict of interest

The authors have no conflict of interest.

Acknowledgements

The authors gratefully acknowledge the financial support from the National Natural Science Foundation of China under Project No. 11502094.

Appendix A. Supplementary material

Supplementary data associated with this article can be found, in the online version, at https://doi.org/10.1016/j.jbiomech.2017.09.027.

References

Bagchi, P., 2007. Mesoscale simulation of blood flow in small vessels. Biophys. J. 92, 1858–1877.
Bagchi, P., Johnson, P.C., Popel, A.S., 2005. Computational fluid dynamic simulation of aggregation of deformable cells in a shear flow. J. Biomech. Eng. 127, 1070–1080.
Bagchi, P., Kalluri, R.M., 2009. Dynamics of nonspherical capsules in shear flow. Phys. Rev. E 80, 016307.
Bagchi, P., Kalluri, R.M., 2011. Dynamic rheology of a dilute suspension of elastic capsules: effect of capsule tank-treading, swinging and tumbling. J. Fluid Mech. 669, 498–526.
Balogh, P., Bagchi, P., 2017. A computational approach to modeling cellular-scale blood flow in complex geometry. J. Comput. Phys. 334, 280–307.
Chandran, K.B., Yoganathan, A.P., Rittgers, S.E., 2007. Biofluid Mechanics: The Human Circulation. CRC/Taylor & Francis.
Dao, M., Lim, C.T., Suresh, S., 2003. Mechanics of the human red blood cell deformed by optical tweezers. J. Mech. Phys. Solids 51, 2259–2280.
Doddi, S.K., Bagchi, P., 2009. Three-dimensional computational modeling of multiple deformable cells flowing in microvessels. Phys. Rev. E 79, 046318.
Dupire, J., Socol, M., Viallat, A., 2012. Full dynamics of a red blood cell in shear flow. PNAS 109, 20808–20813.
Español, P., Revenga, M., 2003. Smoothed dissipative particle dynamics. Phys. Rev. E 67, 026705.
Evans, E., Fung, Y.C., 1972. Improved measurements of the erythrocyte geometry. Microvasc. Res. 4, 335–347.
Fedosov, D.A., Caswell, B., Karniadakis, G.E., 2010. Systematic coarse-graining of spectrin-level red blood cell models. Comput. Meth. Appl. Mech. Eng. 199, 1937–1948.
Fedosov, D.A., Noguchi, H., Gompper, G., 2013. Multiscale modeling of blood flow: from single cells to blood rheology. Biomech. Model Mechanobiol. 13, 239–258.
Gong, X.B., Sugiyama, K., Takagi, S., Matsumoto, Y., 2009. The deformation behavior of multiple red blood cells in a capillary vessel. J. Biomech. Eng. 131, 074504.
Groot, R.D., Warren, P.B., 1997. Dissipative particle dynamics: bridging the gap between atomistic and mesoscopic simulation. J. Chem. Phys. 107, 4423–4435.
Helin, L., Thais, L., Mompean, G., 2009. Numerical simulation of viscoelastic dean vortices in a curved duct. J. Non-Newton. Fluid Mech. 156, 84–94.
Hochmuth, R.M., 1987. Erythrocyte membrane elasticity and viscosity. Ann. Rev. Physiol. 49, 209–219.
Hosseini, S.M., Feng, J.J., 2009. A particle-based model for the transport of erythrocytes in capillaries. Chem. Eng. Sci. 64, 4488–4497.
Hou, H.W., Warkiani, M.E., Khoo, B.L., Li, Z.R., Soo, R.A., Tan, D.S.W., Lim, W.T., Han, J., Bhagat, A.A.S., Lim, C.T., 2013. Isolation and retrieval of circulating tumor cells using centrifugal forces. Sci. Rep. 3, 1259.
Kaoui, B., Biros, G., Misbah, C., 2009. Why do red blood cells have asymmetric shapes even in a symmetric flow? Phys. Rev. Lett. 103, 188101.
Konoura, C., Yagi, T., Nakamura, M., Iwasaki, K., Qian, Y., Okuda, S., Yoshitake, A., Shimizu, H., Yozu, R., Umezu, M., 2013. Numerical analysis of blood flow distribution in 4-and 3-branch vascular grafts. J. Art. Organs 16, 157–163.
Lac, E., Barthes-Biesel, D., Pelekasis, N.A., Tsamopoulos, J., 2004. Spherical capsules in three-dimensional unbounded stokes flows: effect of the membrane constitutive law and onset of buckling. J. Fluid Mech. 516, 303–334.
Lanotte, L., Mauer, J., Mendez, S., Fedosov, D.A., Fromental, J.M., Claveria, V., Nicoud, F., Gompper, G., Abkarian, M., 2016. Red cells' dynamic morphologies govern blood shear thinning under microcirculatory flow conditions. PNAS 113, 8207.
Lee, K.E., Parker, K.H., Caro, C.G., Sherwin, S.J., 2008. The spectral/hp element modelling of steady flow in non-planar double bends. Int. J. Numer. Meth. Fluids 57, 519–529.
Li, H., Ye, T., Lam, K.Y., 2014. Computational analysis of dynamic interaction of two red blood cells in a capillary. Cell Biochem. Biophys. 69, 673–680.
Liu, Y.L., Liu, W.K., 2006. Rheology of red blood cell aggregation by computer simulation. J. Comput. Phys. 220, 139–154.
Liu, Y.L., Zhang, L., Wang, X., Liu, W.K., 2004. Coupling of Navier-Stokes equations with protein molecular dynamics and its application to hemodynamics. Int. J. Numer. Meth. Fluids 46, 12.
Luo, Z.Y., Wang, S.Q., He, L., Xu, F., Bai, B.F., 2013. Inertia-dependent dynamics of three-dimensional vesicles and red blood cells in shear flow. Soft Matter 9, 9651–9660.
McWhirter, J.L., Noguchi, H., Gompper, G., 2009. Flow-induced clustering and alignment of vesicles and red blood cells in microcapillaries. PNAS 106, 6039–6043.
McWhirter, J.L., Noguchi, H., Gompper, G., 2011. Deformation and clustering of red blood cells in microcapillary flows. Soft Matter 7, 10967–10977.
Morris, J.P., 2000. Simulating surface tension with smoothed particle hydrodynamics. Int. J. Numer. Meth. Fluids 33, 333–353.
Morris, J.P., Fox, P.J., Zhu, Y., 1997. Modeling low reynolds number incompressible flows using sph. J. Comput. Phys. 136, 214–226.
Morris, L., Delassus, P., Callanan, A., Walsh, M., Wallis, F., Grace, P., McGloughlin, T., 2005. 3-d numerical simulation of blood flow through models of the human aorta. J. Biomech. Eng. 127, 767–775.
Nardi, A., Avrahami, I., 2017. Approaches for treatment of aortic arch aneurysm, a numerical study. J. Biomech. 50, 158–165.
Noguchi, H., 2009. Swinging and synchronized rotations of red blood cells in simple shear flow. Phys. Rev. E 80.
Noguchi, H., 2010. Dynamic modes of microcapsules in steady shear flow: effects of bending and shear elasticities. Phys. Rev. E 81, 056319.
Noguchi, H., Gompper, G., 2005. Vesicle dynamics in shear and capillary flows. J. Phys.: Condens. Matter 17, S3439–S3444.
Noguchi, H., Gompper, G., Schmid, L., Wixforth, A., Franke, T., 2010. Dynamics of fluid vesicles in flow through structured microchannels. EPL 89, 28002.
Peskin, C.S., 2002. The immersed boundary method. Acta Numer. 11, 1–39.
Pozrikidis, C., 2005. Axisymmetric motion of a file of red blood cells through capillaries. Phys. Fluids 17, 031503.
Pries, A.R., Neuhaus, D., Gaehtgens, P., 1992. Blood viscosity in tube flow: dependence on diameter and hematocrit. Am. J. Physiol. 263, H1770–H1778.
Shahcheraghi, N., Dwyer, H.A., Cheer, A.Y., Barakat, A.I., Rutaganira, T., 2002. Unsteady and three-dimensional simulation of blood flow in the human aortic arch. J. Biomech. Eng. 124, 378–387.
Sollier, E., Rostaing, H., Pouteau, P., Fouillet, Y., Achard, J.L., 2009. Passive microfluidic devices for plasma extraction from whole human blood. Sen. Act. B Chem. 141, 617–624.
Sui, Y., Chew, Y.T., Roy, P., Cheng, Y.P., Low, H.T., 2008. Dynamic motion of red blood cells in simple shear flow. Phys. Fluids 20, 112106.

Sun, D.K., Xiang, N., Jiang, D., Chen, K., Yi, H., Ni, Z.H., 2013. Multi-relaxation time lattice boltzmann simulation of inertial secondary flow in a curved microchannel. Chin. Phys. B 22, 114704.
Tahiri, N., Biben, T., Ez-Zahraouy, H., Benyoussef, A., Misbah, C., 2013. On the problem of slipper shapes of red blood cells in the microvasculature. Microvas. Res. 85, 40–45.
Takagi, S., Yamada, T., Gong, X.B., Matsumoto, Y., 2009. The deformation of a vesicle in a linear shear flow. J. Appl. Mech. 76, 021207.
Vahidkhah, K., Balogh, P., Bagchi, P., 2016. Flow of red blood cells in stenosed microvessels. Sci. Rep. 6, 28194.
Vázquez-Quesada, A., Ellero, M., Español, P., 2009. Smoothed particle hydrodynamic model for viscoelastic fluids with thermal fluctuations. J. Chem. Phys. 130, 034901.
Vincent, P.E., Plata, A.M., Hunt, A.A.E., Weinberg, P.D., Sherwin, S.J., 2011. Blood flow in the rabbit aortic arch and descending thoracic aorta. J. R. Soc. Interface 8, 1708–1719.
Wang, T., Pan, T.W., Xing, Z.W., Glowinski, R., 2009. Numerical simulation of rheology of red blood cell rouleaux in microchannels. Phys. Rev. E 79, 041916.
Warkiani, M.E., Guan, G.F., Luan, K.B., Lee, W.C., Bhagat, A.A.S., Chaudhuri, P.K., Tan, D.S.W., Lim, W.T., Lee, S.C., Chen, P.C.Y., Lim, C.T., Han, J., 2014a. Slanted spiral microfluidics for the ultra-fast, label-free isolation of circulating tumor cells. Lab Chip 14, 128–137.
Warkiani, M.E., Khoo, B.L., Tan, D.S.W., Bhagat, A.A.S., Lim, W.T., Yap, Y.S., Lee, S.C., Soo, R.A., Han, J., Lim, C.T., 2014b. An ultra-high-throughput spiral microfluidic biochip for the enrichment of circulating tumor cells. Analyst 139, 3245–3255.
Warkiani, M.E., Khoo, B.L., Wu, L., Tay, A.K.P., Bhagat, A.A.S., Han, J., Lim, C.T., 2016. Ultra-fast, label-free isolation of circulating tumor cells from blood using spiral microfluidics. Nat. Prot. 11, 134–148.
Xu, D., Kaliviotis, E., Munjiza, A., Avital, E., Ji, C., Williams, J., 2013. Large scale simulation of red blood cell aggregation in shear flows. J. Biomech. 46, 1810–1817.
Xu, J., Wang, X.L., Liu, Y.Q., Gong, X.B., 2014. A cellular scale numerical study of the effect of mechanical properties of erythrocytes on the near-wall motion of platelets. Acta Mech. Sin. 30, 274–280.
Yazdani, A.Z.K., Bagchi, P., 2011. Phase diagram and breathing dynamics of a single red blood cell and a biconcave capsule in dilute shear flow. Phys. Rev. E 84, 026314.
Ye, T., Li, H., Lam, K.Y., 2010. Modeling and simulation of microfluid effects on deformation behavior of a red blood cell in a capillary. Microvasc. Res. 80, 453–463.
Ye, T., Phan-Thien, N., Khoo, B.C., Lim, C.T., 2013. Stretching and relaxation of malaria-infected red blood cells. Biophys. J. 105, 1103–1109.
Ye, T., Phan-Thien, N., Khoo, B.C., Lim, C.T., 2014a. A file of red blood cells in tube flow: a three-dimensional numerical study. J. Appl. Phys. 116, 124703.
Ye, T., Phan-Thien, N., Khoo, B.C., Lim, C.T., 2014b. Numerical modelling of a healthy/malaria-infected erythrocyte in shear flow using dissipative particle dynamics method. J. Appl. Phys. 115, 224701.
Ye, T., Phan-Thien, N., Lim, C.T., Peng, L., Shi, H.X., 2017. Hybrid smoothed dissipative particle dynamics and immersed boundary method for simulation of red blood cells in flows. Phys. Rev. E 95, 063314.
Zhang, J., 2011. Effect of suspending viscosity on red blood cell dynamics and blood flows in microvessels. Microcirculation 18, 562–573.
Zhang, J., Johnson, P.C., Popel, A.S., 2008. Red blood cell aggregation and dissociation in shear flows simulated by lattice Boltzmann method. J. Biomech. 41, 47–55.
Zhang, J., Johnson, P.C., Popel, A.S., 2009. Effects of erythrocyte deformability and aggregation on the cell free layer and apparent viscosity of microscopic blood flows. Microvas. Res. 77, 265–272.